Composites: Part B 40 (2009) 572–583

Contents lists available at ScienceDirect

Composites: Part B

journal homepage: www.elsevier.com/locate/compositesb

Transverse impact damage and energy absorption of 3-D multi-structured knitted composite

Baozhong Sun [a], Dongmei Hu [a], Bohong Gu [a,b,*]

[a] College of Textiles, Donghua University, Shanghai 201620, China
[b] Department of Textile Engineering, Zhongyuan Institute of Technology, Zhengzhou, Henan Province 450007, China

ARTICLE INFO

Article history:
Received 25 October 2008
Received in revised form 16 November 2008
Accepted 9 December 2008
Available online 9 May 2009

Keywords:
A. 3-Dimensional reinforcement (3-D Multi-structured knitted composite)
Unit-cell
B. Impact behaviour (Transverse impact)
C. Finite element analysis (FEA)

ABSTRACT

Knitted composites have higher failure deformation and energy absorption capacity under impact than other textile structural composites because of the yarn loop structures in knitted performs. Here we report the transverse impact behavior of a new kind of 3-D multi-structured knitted composite both in experimental and finite element simulation. The knitted composite is composed of two knitted fabrics: biaxial warp knitted fabric and interlock knitted fabric. The transverse impact behaviors of the 3-D knitted composite were tested with a modified split Hopkinson pressure bar (SHPB) apparatus. The load–displacement curves and damage morphologies were obtained to analyze the energy absorptions and impact damage mechanisms of the composite under different impact velocities. A unit-cell model based on the microstructure of the 3-D knitted composite was established to determine the composite deformation and damage when the composite impacted by a hemisphere-ended steel rod. Incorporated with the unit-cell model, a elasto-plastic constitute equation of the 3-D knitted composite and the critical damage area (CDA) failure theory of composites have been implemented as a vectorized user defined material law (VUMAT) for ABAQUS/Explicit. The load–displacement curves, impact deformations and damages obtained from FEM are compared with those in experimental. The good agreements of the comparisons prove the validity of the unit-cell model and user-defined subroutine VUMAT. This manifests the applicability of the VUMAT to characterization and design of the 3-D multi-structured knitted composite structures under other impulsive loading conditions.

1. Introduction

Knitted fabric composites have been recognized as more competitive in impact energy absorption than other 3-D textile structural composites. The yarn loop structures of knitted fabrics will have large deformation when the knitted composite under impulsive loading. Just like the woven fabric, the longitudinal direction of knitted fabric is called wale direction and the transverse direction is named course direction.

Investigations on mechanical properties of knitted composite so far are mainly focused on the quasi-static loading conditions. As for the mechanical behaviors under dynamic or impulsive loading, Pandita et al. [1] investigated the impact properties of weft-knitted fabric composites based on their fracture toughness and tensile properties. Khondker et al. [2–5] published a series of papers about the mechanical properties of knitted composites. These results were important to study and design knitted composites. Ramakrishna et al. [6] conducted drop test of knitted glass fiber reinforced polypropylene laminates and understood both peak load and puncture energy were sensitive to the stitch density, number of plies and imposed strain rate. Kang et al. [7,8] discussed the mechanical and impact properties of multi-axial warp knit fabric reinforced composite laminates. Cox et al. [9] studied the energy absorption of knitted composites under tensile loading. Lam et al. [10] examined the energy-absorption behavior and mechanism of various thermoplastic cellular textile composites with flat-topped grid-domed cellular structure. Putnoki et al. [11] used instrumented falling weight impact tests to determine the dynamic perforation impact behavior of knitted fabric glass fiber reinforced PET composites produced from commingled yarn. Sugun et al. [12] tested the drop impact property of six types of weft rib knit fabric reinforced composites developed on a flat bed hand knitting machine from E-glass rovings. Zhou et al. [13] studied the low-velocity impact energy absorption characteristics of composites reinforced by the multi-axial warp knitted (MWK) structures with double loop pillar stitch and common tricot stitch. Huang et al. [14] analyzed the progressive failure process of laminated composites with knitted fabric subjected to a bending load, based on the classical lamination theory and a bridging micromechanics model. Sun

* Corresponding author. Address: Department of Textile Engineering, Zhongyuan Institute of Technology, Zhengzhou, Henan Province 450007, China. Tel.: +86 21 67792661, +86 371 67698880; fax: +86 21 67792627, +86 371 62506970.
E-mail address: gubh@dhu.edu.cn (B. Gu).

1359-8368/$ - see front matter © 2009 Elsevier Ltd. All rights reserved.
doi:10.1016/j.compositesb.2008.12.005

et al. [15] tested the compressive properties of multi-axial multi-layer E-glass/epoxy warp knitted (MMWK) composites at quasi-static and high strain rates loadings. The results indicate that the stress strain curves are rate sensitive, and compressive stiffness, maximum compressive stress and corresponding compressive strain are also sensitive to the strain rate.

This paper presents the impact responses and energy absorption analysis of a new kind of multi-structured knitted composite. The knitted composite is composed of two kinds of knitted fabrics: biaxial warp knitted fabric and interlock knitted fabric. The biaxial warp knitted fabric provides high tension modulus and strength, and the interlock knitted fabric provides large deformation. The knitted composite combines the double-faced interlock knitted fabric and biaxial knitted fabric together to have both large deformation and high in-plane stiffness. A unit-cell model which is derived from the microstructure of the 3-D knitted composite was developed to analyze impact energy absorption, deformation and damage of the composite panel under transverse impact. A 3-D elasto-plastic constitutive model and critical damage area (CDA) failure theory of the knitted composite were implemented as a user-defined material law (VUMAT) for commercial finite element (FE) software package ABAQUS/Explicit. The ABAQUS/Explicit was incorporated with the user-defined subroutine VUMAT to calculate transverse impact behavior of the 3-D knitted composite. The FEM results have been verified with experimental results to show the validity of the unit-cell approach and user-defined VUMAT model.

2. Composite specimen and transverse impact

A modified split Hopkinson pressure bar (SHPB) apparatus was used to test the transverse impact behavior of the 3-D biaxial spacer weft knitted composite panel. The detailed principle of the apparatus could be found in elsewhere [16–18].

Two knitted fabrics are inter-layered each other to form a hybrid knitted structure. One knitted fabric is double-faced interlock knitted fabric. The sketch architecture of the knitted fabric is shown in Fig. 1. Fig. 2 shows the fabric surface. The fabric was made of basalt filament tows. The basalt filament tows were manufactured by Hengdian Group Shanghai Russia and Gold Basalt Fiber Co., Ltd. The specification of the knitted fabric and basalt yarns are listed in Tables 1 and 2. Fig. 3 is the surface of another knitted fabric, i.e., biaxial warp knitted fabric. The sketch of the knitted fabric could be found elsewhere [19]. From the structural geometry point of view, the fabric consists of warp (0°) and weft (90°) yarns held together by a chain or tricot stitch through the thickness of the fabric. Compared with woven fabric, the warp and weft yarn in the knitted fabric are not interlaced each other to from a stable structure. The binder yarns (whiter color in Fig. 3) combines the un-interlaced warp and weft yarns together. The stability of the biaxial knitted fabric is from the bindings of knitted yarn loops. The non-crimp features of the warp and weft yarns lead the high in-plane stiffness and strength. The fabric is also made of basalt filament tows. The specification of the biaxial knitted fabric is listed in Table 3.

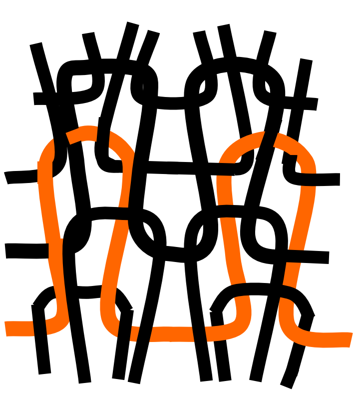

Fig. 1. Architecture of double-faced interlock knitted fabric.

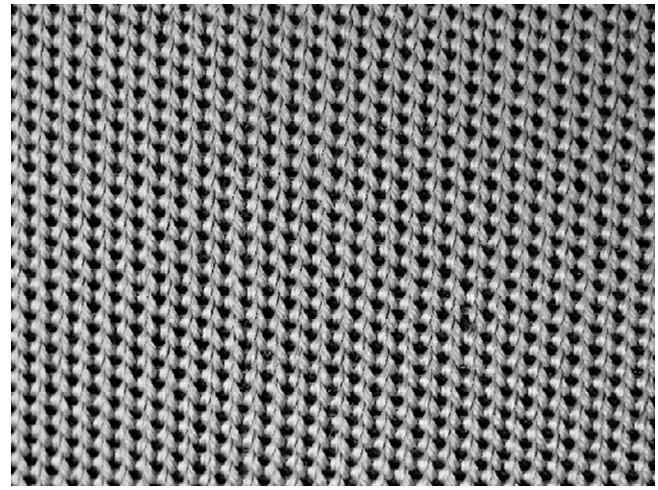

Fig. 2. Surface of double-faced interlock knitted fabric made of basalt filament tows.

Table 1
Parameters of double-faced interlock knitted fabric.

Yarns	Basalt filament tows
Parameters	
Linear density of knit yarn (tex)	280
Course loop density (courses/10 cm)	58
Wale loop density (wales/10 cm)	59

Table 2
Parameters of biaxial warp knitted fabric.

Yarns	Continuous basalt fiber
Parameters	
Linear density of Warp yarn (tex)	1000
Linear density of Weft yarn (tex)	1200
Warp yarn density (wales/10 cm)	39
Weft yarn density (courses/10 cm)	33

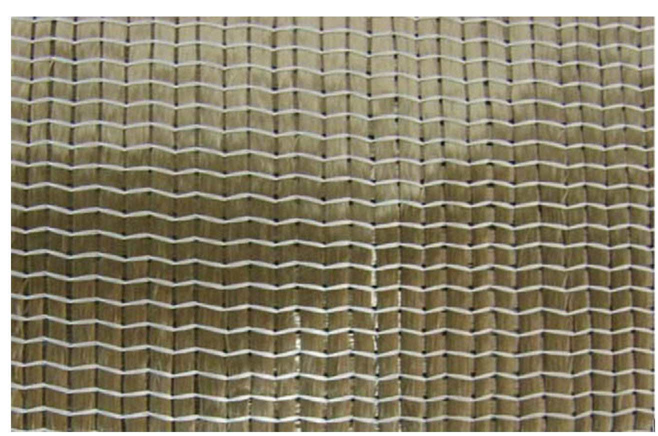

Fig. 3. Surface of biaxial warp knitted fabric made of basalt filament tows.

Table 3
Parameters of connecting yarns.

Yarns	Continuous basalt fiber
Parameters	
Linear density of connecting yarn (tex)	280
Warp connecting yarn density (wales/10 cm)	13
Weft connecting yarn density (courses/10 cm)	11

Table 4
Modulus of Interlock stitch fiber and connecting fiber.

	E11 (GPa)	E22 (GPa)	E33 (GPa)	G12 (GPa)	G13 (GPa)	G23 (GPa)	ν_{12}	ν_{23}	ν_{13}
Stitched fiber	110	98	98	0.4	0.4	0.38	0.2	0.18	0.2
Warp	100	93	93	0.34	0.34	0.32	0.24	0.21	0.24
Weft	102	95	95	0.35	0.35	0.33	0.23	0.2	0.23

Four pieces of fabrics were used in manufacturing the multi-structured sandwiched knitted composite. Two layers of biaxial knitted fabric were laid in the top and bottom surface, respectively. Two layers of double-faced interlock knitted fabrics were sandwiched between the two biaxial warp knitted fabrics. Then the fabrics were stitched together as a multi-structured knitted fabric. Table 4 lists the specifications of the stitching tow. The sketch of the multi-structured knitted fabric is shown in Fig. 4.

Vinyl ester resin (Type RF-1001, manufactured by Shanghai Sino Composite Co., Ltd.), the viscosity of which is 0.45 Pas at room temperature, was used to manufacture the knitted composite. Butanone and acrylic cobalt were used as curing agent and catalyst, respectively. The proportion of resin, curing agent, and catalyst was 100:1:0.5 by weight.

The sketch of the composite manufacturing is shown in Fig. 5. The resin solution was injected into knitted fabric through VARTM (vacuum assisted resin transfer molding) process and cured for 24 h at room temperature followed by post curing in an oven at 80 °C for 4 h. The fiber volume fraction is about 40%. The surface photograph of the composite is shown in Fig. 6.

The composite plate was cut with high pressure water jet along wale and course direction of the knitted fabric, respectively. The size of composite coupon is 120 × 30 × 5 mm and could be shown in Fig. 7.

The load–displacement curves of the composite coupons under transverse impact could be obtained with the modified SHPB apparatus to analyze the impact energy absorption and to verify the finite element calculation results. The impact velocity was controlled by adjusting gas pressure of the SHPB apparatus, and was 17.5, 20.0 and 22.5 m/s, respectively.

3. Unit-cell modeling and FE formulation

3.1. Unit-cell model

In order to simplify the unit-cell characterization, only 1/2 unit cell of the knitted fabric is used in finite element calculation because of the symmetry of the unit-cell along thickness direction. Fig. 8 is the unit-cell of the multi-structured knitted composite.

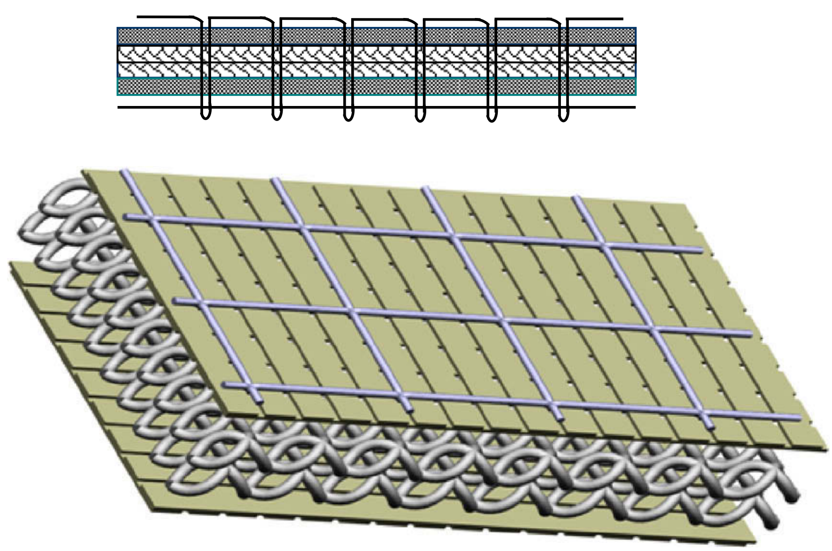

Fig. 4. Sketch of multi-structured sandwiched knitted fabric.

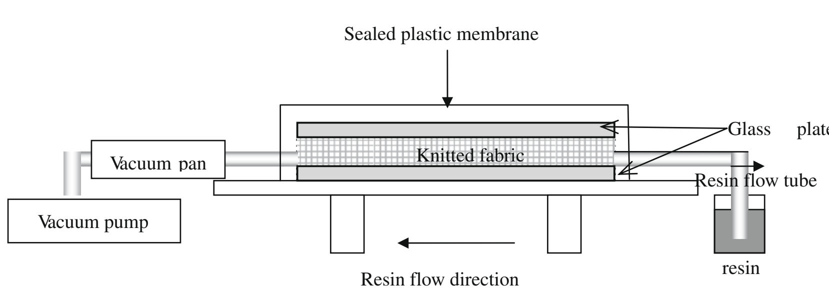

Fig. 5. Sketch of composite manufacturing with VARTM technique.

Each yarn has its own local Cartesian coordinate, 1-2-3, which along the yarn's axis (1-direction), perpendicular to the axis (2-direction) and 3-direction. In the unit-cell model, the bond between fiber tows and resin is regarded as perfect, i.e., there is not debonding at the interface.

The resin in composite is assumed as isotropic material, the compliances matrix is:

$$[S]_m = \begin{bmatrix} 1/E_m & -\nu_m/E_m & -\nu_m/E_m & 0 & 0 & 0 \\ -\nu_m/E_m & 1/E_m & -\nu_m/E_m & 0 & 0 & 0 \\ -\nu_m/E_m & -\nu_m/E_m & 1/E_m & 0 & 0 & 0 \\ 0 & 0 & 0 & 1/G_m & 0 & 0 \\ 0 & 0 & 0 & 0 & 1/G_m & 0 \\ 0 & 0 & 0 & 0 & 0 & 1/G_m \end{bmatrix} \tag{1}$$

For the unit cell, assume $[S]$ are the compliance matrixes of continuous basalt fiber in the local coordinate. The tows can be regarded as transverse-isotropic materials. Then:

$$[S] = \begin{bmatrix} S_{11} & S_{12} & S_{12} & 0 & 0 & 0 \\ S_{12} & S_{22} & S_{23} & 0 & 0 & 0 \\ S_{12} & S_{23} & S_{22} & 0 & 0 & 0 \\ 0 & 0 & 0 & 2(S_{22}-S_{23}) & 0 & 0 \\ 0 & 0 & 0 & 0 & S_{55} & 0 \\ 0 & 0 & 0 & 0 & 0 & S_{55} \end{bmatrix} \tag{2}$$

For the warp yarns (tows) in the unit-cell (shown in Fig. 8), they are in straight line because there are not interlace with weft yarns. The local coordinate is identical with the X-axis in global coordinate.

Then: $[\bar{S}]_1 = [S]$

The straight weft yarns in Fig. 8 are perpendicular to the X-axis in global coordinate. The compliance matrix for the weft yarns is:

$$[\bar{S}]_2 = [T_2]^{-1}[S][T_2] \tag{3}$$

where $[T_2]$ is strain transformation matrix.

$$[T] = \begin{bmatrix} l_1^2 & m_1^2 & n_1^2 & 2m_1n_1 & 2l_1n_1 & 2l_1m_1 \\ l_2^2 & m_2^2 & n_2^2 & 2m_2n_2 & 2l_2n_2 & 2l_2m_2 \\ l_3^2 & m_3^2 & n_3^2 & 2m_3n_3 & 2l_3n_3 & 2l_3m_3 \\ 2l_2l_3 & 2m_2m_3 & 2n_2n_3 & 2(m_2n_3+m_3n_2) & 2(l_2n_3+l_3n_2) & 2(l_2m_3+l_3m_2) \\ 2l_1l_3 & 2m_1m_3 & 2n_1n_3 & 2(m_1n_3+m_3n_1) & 2(l_1n_3+l_3n_1) & 2(l_1m_3+l_3m_1) \\ 2l_1l_2 & 2m_1m_2 & 2n_1n_2 & 2(m_1n_2+m_2n_1) & 2(l_1n_2+l_2n_1) & 2(l_1m_2+l_2m_1) \end{bmatrix} \tag{4}$$

The elements of $[T_2]$ are:

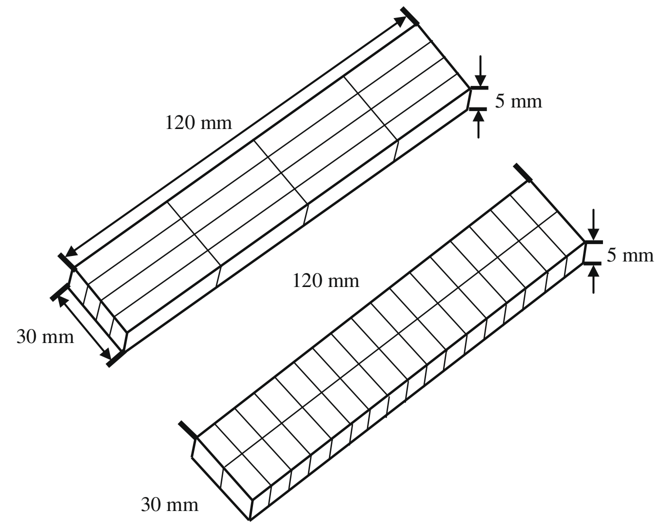

Fig. 7. Size of knitted composite coupon (upper: wale direction; lower: course direction).

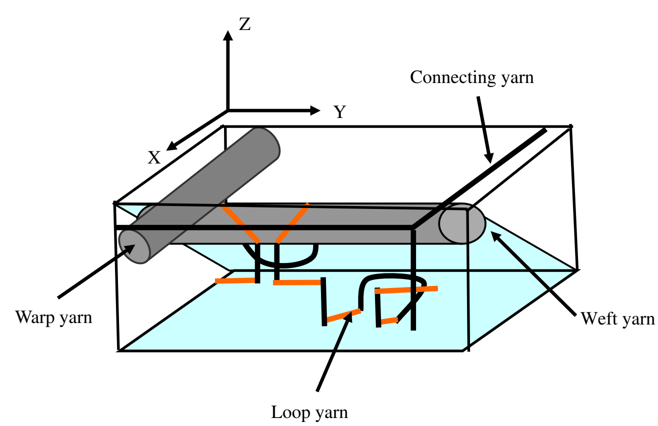

Fig. 8. Half part unit-cell model of 3-D multi-structured knitted fabric.

$l_1 = 0,\quad l_2 = -1,\quad l_3 = 0,\quad m_1 = 1,\quad m_2 = 0,\quad m_3 = 0,$
$n_1 = 0,\quad n_2 = 0,\quad n_3 = 1$

For the connecting yarns parallel to x axis in the unit-cell (shown in Fig. 8), the local coordinate and the global coordinate is dentical. Then: $[\bar{S}]_3 = [S]$

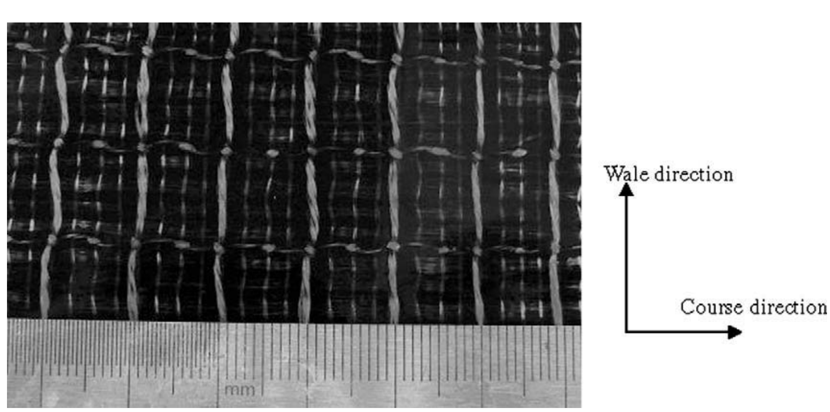

Fig. 6. Surface photograph of the multi-structured knitted composite.

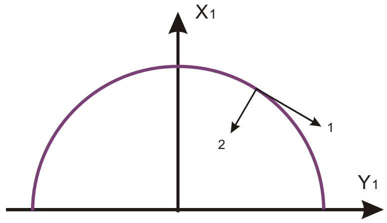

Fig. 9. Schematic diagram of the top loop in double-faced interlock knitted fabric.

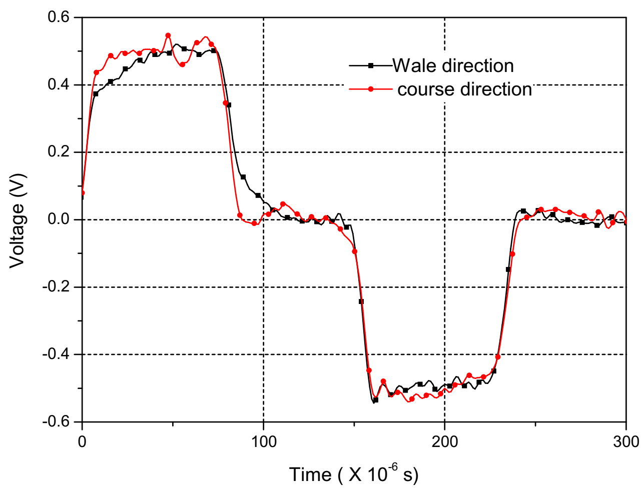

Fig. 10. Typical signal of stress wave under transverse impact.

Table 5
Strength of f Interlock stitch fiber and connecting fiber.

	XT (MPa)	XC (MPa)	YT (MPa)	YC (MPa)	SS12 (MPa)	SS23 (MPa)
Stitched fiber	4800	4800	4000	4000	2000	2000
Warp	4200	4200	3500	3500	1700	1700
Weft	4500	4500	3800	3800	1800	1800

Table 6
Modulus and strength of matrix.

E (GPa)	G (GPa)	ν	XT (MPa)	XC (MPa)	SS (MPa)
3.65	1.35	0.35	78	146	156

The compliance matrix for the connecting yarn y is

$$[\bar{S}]_4 = [T_4]^{-1}[S][T_4] \tag{5}$$

where $[T_4]$ is strain transformation matrix, and the elements of $[T_4]$ are

$$l_1 = 0, \quad l_2 = -1, \quad l_3 = 0, \quad m_1 = 1, \quad m_2 = 0, \quad m_3 = 0,$$
$$n_1 = 0, \quad n_2 = 0, \quad n_3 = 1$$

The compliance matrix for the connecting yarn y is

$$[\bar{S}]_5 = [T_5]^{-1}[S][T_5] \tag{6}$$

where $[T_5]$ is strain transformation matrix, and the elements of $[T_5]$ are

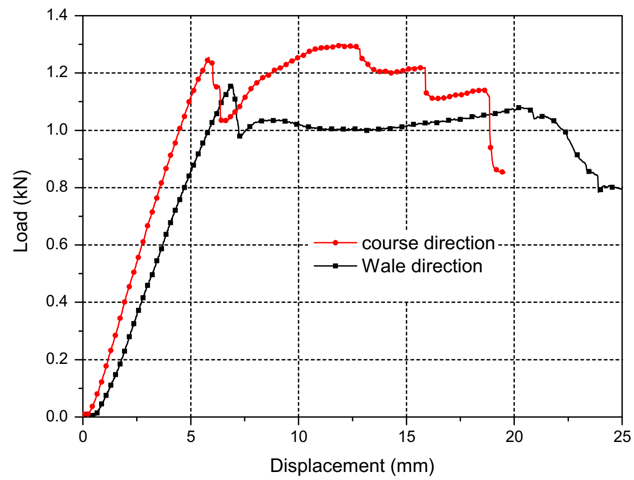

Fig. 11. Load–displacement curves under quasi-static loading along course and wale direction.

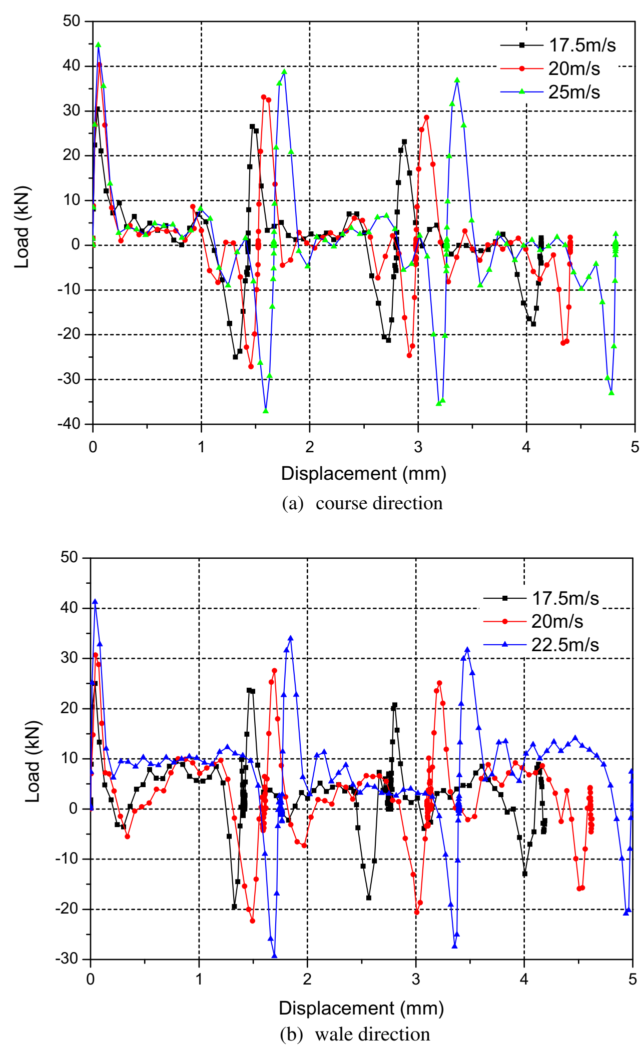

Fig. 12. Experimental load–displacement curves under different impact velocities.

$$l_1 = 0, \quad l_2 = 0, \quad l_3 = -1, \quad m_1 = 0, \quad m_2 = 1, \quad m_3 = 0,$$
$$n_1 = 1, \quad n_2 = 0, \quad n_3 = 0$$

The loop yarn is composed of three parts: the upper loop, three straight lines and the lower loop. As shown in Fig. 8, the upper loop is simplified to one half-circle line and four straight lines. The lower loop is same to the upper loop.

The half-circle line is shown in Fig. 9. We can get a local part of the loop line. The compliance matrix for micro-part of the loop line is

$$[S]_{6\alpha_j} = [T_{6\alpha_j}][\bar{S}_6][T_{6\alpha_j}]^{-1} \tag{7}$$

The compliance matrix for the whole half-circle line is

$$[S_{6\alpha}] = \frac{1}{\pi}\int_{-\pi/2}^{\pi/2}[S]_{6\alpha_j}\mathrm{d}\alpha_j \tag{8}$$

In x–y plane it can be converted to

$$[S] = [T_6][S_{6\alpha}][T_6]^{-1} \tag{9}$$

The elements of $[T_6]$ are:

$$l_1 = \sin\alpha,\quad l_2 = -\cos\alpha,\quad l_3 = 0,$$
$$m_1 = \cos\alpha,\quad m_2 = -\sin\alpha,\quad m_3 = 0,$$
$$n_1 = 0,\quad n_2 = 0,\quad n_3 = 1$$

If the angle between the upper half-circle to x axes is θ_1,

Then the elements of $[T_6]$ are:

$$l_1 = \cos\theta_1,\quad l_2 = 0,\quad l_3 = \sin\theta_1,$$
$$m_1 = 0,\quad m_2 = 1,\quad m_3 = 0,$$
$$n_1 = -\sin\theta_1,\quad n_2 = 0,\quad n_3 = \cos\theta_1$$

The compliance matrix for the two yarns which parallel to z axes of upper loop is:

$$[\bar{S}]_7 = [T_7]^{-1}[S][T_7] \quad \text{and} \quad [\bar{S}]_8 = [T_8]^{-1}[S][T_8] \tag{10}$$

where $[T_7]$ and $[T_8]$ are strain transformation matrix, and the elements of $[T_7]$ and $[T_8]$ are both as:

$$l_1 = 0,\quad l_2 = 0,\quad l_3 = -1,\quad m_1 = 0,\quad m_2 = 1,\quad m_3 = 0,$$
$$n_1 = 1,\quad n_2 = 0,\quad n_3 = 0$$

The compliance matrix for the two straight yarns parallel to X–Zplane of upper loop is:

$$[\bar{S}]_9 = [T_9]^{-1}[S][T_9] \quad \text{and} \quad [\bar{S}]_{10} = [T_{10}]^{-1}[S][T_{10}] \tag{11}$$

If the angle between the yarn and y axes is $\pm\theta$,

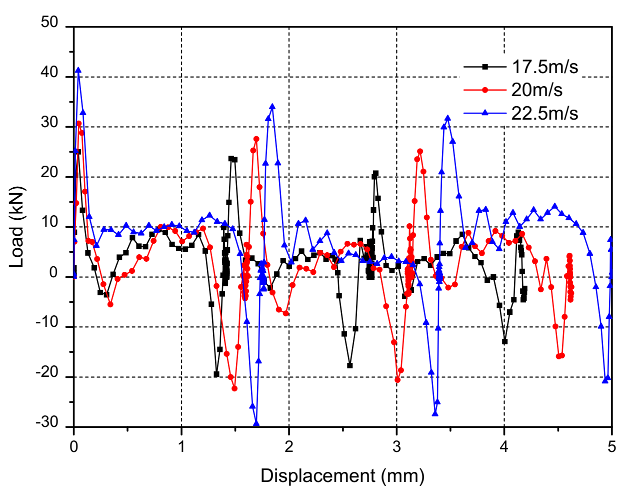

(a) course direction

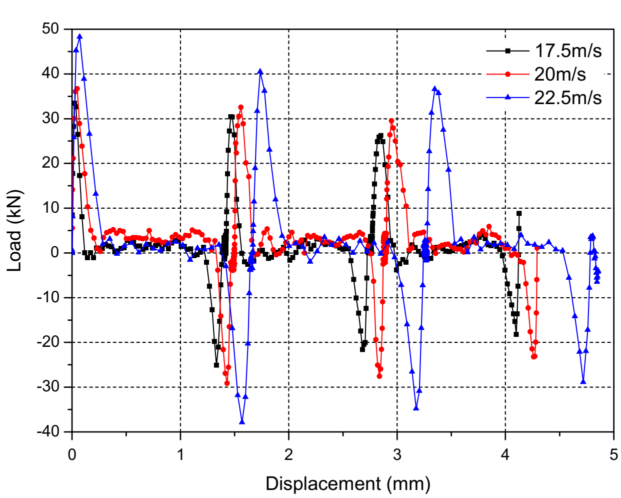

(b) wale direction

Fig. 13. FE load–displacement curves under different impact velocities.

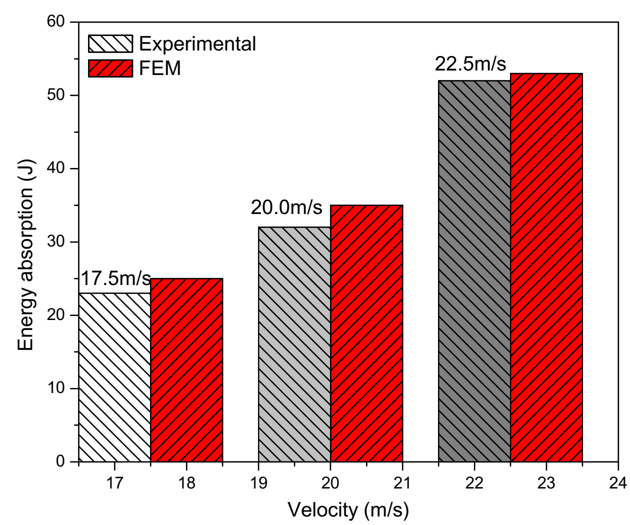

(a) warp (wale) direction

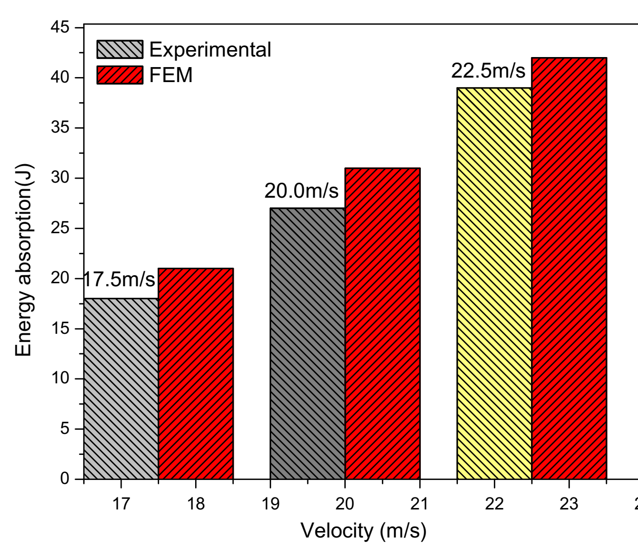

(b) weft (course) direction

Fig. 14. Comparison of energy absorption along wale and course direction.

Then the elements of $[T_9]$ and $[T_{10}]$ are:

$$l_1 = \cos\theta_x,\quad l_2 = -\sin\theta_x,\quad l_3 = 0,$$
$$m_1 = \sin\theta_x,\quad m_2 = \cos\theta_x,\quad m_3 = 0,$$
$$n_1 = 0,\quad n_2 = 0,\quad n_3 = 1$$

and $[T_{10}]$ are:

$$l_1 = \cos\theta_x,\quad l_2 = \sin\theta_x,\quad l_3 = 0,$$
$$m_1 = -\sin\theta_x,\quad m_2 = \cos\theta_x,\quad m_3 = 0,$$
$$n_1 = 0,\quad n_2 = 0,\quad n_3 = 1$$

The lower half-circle line is similar to upper half-circle line. If the angle between the lower half-circle to x axes is $-\theta_x$, the compliance matrix for this part is:

$$[S]_{11\alpha_j} = [T_{11\alpha_j}][\bar{S}_{11}][T_{11\alpha_j}]^{-1} \tag{12}$$

Then the compliance matrix for the whole half-circle line is:

$$[S_{11\alpha}] = \frac{1}{\pi}\int_{-\pi/2}^{\pi/2}[S]_{11\alpha_j}\mathrm{d}\alpha_j \tag{13}$$

In x–y plane it can be converted to

$$[S] = [T_{11}][S_{11\alpha}][T_{11}]^{-1} \tag{14}$$

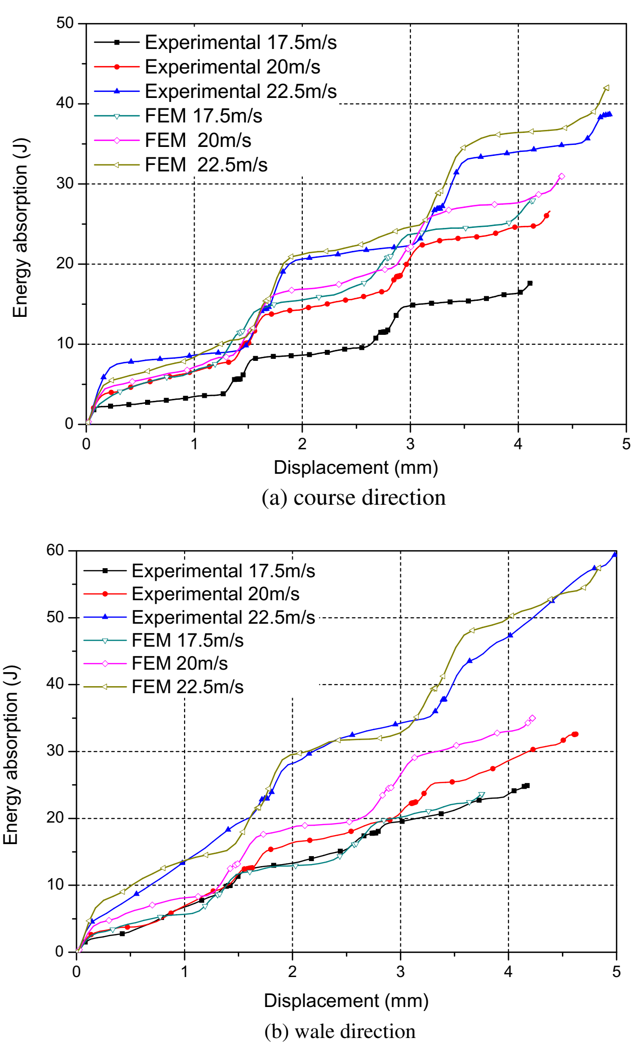

(a) course direction

(b) wale direction

Fig. 15. Comparisons of energy-absorption curves between experimental and theoretical.

The elements of $[T_{11}]$ are:

$$l_1 = -\sin\beta,\quad l_2 = -\cos\beta,\quad l_3 = 0,$$
$$m_1 = \cos\beta,\quad m_2 = -\sin\beta,\quad m_3 = 0,$$
$$n_1 = 0,\quad n_2 = 0,\quad n_3 = 1$$

The compliance matrix for other four straight lines are same to upper line.

The compliance matrix for the two straight yarns parallel to y axes is:

$$[\bar{S}]_{12} = [T_{12}]^{-1}[S][T_{12}],\quad [\bar{S}]_{13} = [T_{13}]^{-1}[S][T_{13}]\quad \text{and}$$
$$[\bar{S}]_{14} = [T_{14}]^{-1}[S][T_{14}] \tag{15}$$

where $[T_{12}]$, $[T_{13}]$ and $[T_{14}]$ are both the strain transformation matrix, and the elements of them are same, i.e.,

$$l_1 = 0,\quad l_2 = -1,\quad l_3 = 0,$$
$$m_1 = 1,\quad m_2 = 0,\quad m_3 = 0,$$
$$n_1 = 0,\quad n_2 = 0,\quad n_3 = 1$$

3.2. Unit-cell homogenization

Under the assumptions of iso-strain, strain can be transformed from the global to the local coordinate system with the following relation:

$$\varepsilon_k^{local} = [T]\varepsilon^{global} \tag{16}$$

where $[T]$ is a transformation matrix.

Elastically, the global–local stress relations are:

$$\sigma_k^{local} = C_k\varepsilon_k^{local} \tag{17}$$
$$\sigma_k^{global} = [T]^T\sigma_k^{local} \tag{18}$$

In order to apply the elasto-plastic model, incremental stresses and strains must be used with the elasto-plastic compliance S^{ep} and stiffness C^{ep}.

$$[S^{ep}] = [S + S^{vp}]\cdot[C^{ep}] = [C^{ep}]^{-1} \tag{19}$$
$$[C^{ep}] = \left[[I] + [C]\cdot[S^{ep}]\right]^{-1}[C] \tag{20}$$

In incremental form:

$$\Delta\varepsilon_k^{local} = [T]\Delta\varepsilon^{global} \tag{21}$$
$$\Delta\sigma_k^{local} = C_k^{ep}\Delta\varepsilon_k^{local} \tag{22}$$

Then:

$$\Delta\sigma_k^{local} = C_k^{ep}\Delta\varepsilon_k^{local} = C_k^{ep}[T]\Delta\varepsilon^{global} \tag{23}$$

and:

$$\Delta\sigma^{global} = \sum_k V_k\Delta\sigma_k^{global} \tag{24}$$

3.3. Failure criteria

Composite failure is determined by not only the stresses present in the material, but also the area where the stresses exceed critical values. This critical area is governed by the composite's interaction length, which can be as low as 1 mm for tape-based composites and up to 100 mm for some 3-D interlock weaves [20]. The CDA criterion is necessary when considering composite failure because a composite will not necessarily fail when a single fiber or even tow, exceeds its maximum stress. Instead, composite failure will occur only when: (1) stresses exceed the local fiber strength, and (2) a critical damage area has reached. The critical area is calculated by applying Tsai-Hahn fiber-bundle theory [21,22], originally proposed by Rosen [23] to tows to calculate the critical interaction length δ.

The critical damaged length (δ) is defined as

$$\delta = 4\gamma_f \left(\frac{X_f}{4\tau}\right)^{\frac{\kappa}{\kappa+1}} \left[\frac{(\kappa+1)L}{2\gamma_f}\right]^{\frac{1}{\kappa+1}} \quad (25)$$

where γ is the tow radius, X_f is the average fiber tension strength, L is the tow length, typically assumed 1 unit length, τ is the matrix yield stress, and κ is the Weibull parameter. As discussed by Rosen [23] and Gucer et al. [24], the κ is the shape parameter of the Weibull distribution of the fiber strength distribution. Value of κ between 2 and 4 correspond to brittle ceramics, whereas a value of 20 is appropriate for a ductile metal. For the E-glass filament yarns, the κ is assumed to be 7.6.

The damage of composite must accord with two conditions. One condition is stresses in material beyond the strength of local fibers. The other is the stress area beyond the *CDA*.

If the *CDA* is square, it equals δ^2. Before the damage of composite, fiber degradation increases with the critical damaged area.

The value of δ determined from Eq. (25) is only used as an approximation because of the assumption required for analysis and variations of the material parameters. For instance, the value of $\delta$for typical graphite/epoxy composites range from 0.025 in. (0.0635 cm) to 0.060 in. (0.1524 cm) [25]. For E-glass/vinyl ester resin composites, δ was found to be about 27 mm.

$$E^i = E_0^i \left[1 - \left(\frac{DA - DA_f^i}{CDA}\right)^2\right] \quad (26)$$

where E^i is the E_{11} Young's Modulus at point i, E_0 is the undamaged modulus, *CDA* is the Critical Damaged Area, *DA* is the current damaged area where the longitudinal stress has exceeded the tension strength of the composite *XT*, and DA_f^i is the value of *DA* when point i exceeds its maximum stress.

4. Numerical simulations

We conducted finite element analysis based on the following software:

Finite element code: ABAQUS/Explicit ver 6.5.1

OS platform: Windows XP®

Subroutine compiling language: Compaq FORTRAN compiler (ver 6.6)

4.1. User's subroutine VUMAT in ABAQUS

User's subroutine VUMAT (vectorized user-defined material law) for ABAQUS/Explicit was used to define the mechanical constitutive behavior and failure theories of the 3-D knitted composite. During FE calculations, ABAQUS/explicit passes information regarding strains distribution to the user's subroutine. The constitutive model in the user's subroutine then gives the stress distribution based on failure theories analysis. The damage state and extent of the 3-D knitted composite will be estimated at the given stress with the CDA failure theory.

4.2. Finite element (FE) models

The FE model includes the incident bar of the Split Hopkinson pressure bar (SHPB) apparatus and the composite specimen. Only 1/2 of the incident bar and specimen were modeled and meshed because of the symmetry of the model. The reduced integration C3D8R brick elements are used for meshing. The element size of the composite is same with the size of the unit cells. There are 60 (length) × 2 (width) × 2 (thickness) elements in wale direction model and the model of the composite in course direction has 14 (length) × 9 (width) × 2 (thickness) elements. The SHPB is regarded as isotropic elastic body (the mechanical parameters of steel have been used in calculation) and explicit time integration option in ABAQUS/Explicit is used in the calculation. In order to reduce the error of simulation, the original impact stress wave in the incident bar was input as the initial loading condition of the FE model. Fig. 10 is the original signal recorded by strain gauge mounted on the incident bar.

The definition of the boundary condition for the incident bar in ABAQUS is to fix the freedom of displacement and rotation except the displacement along longitudinal direction of the bar. The boundary condition for the composite coupon is defined as 'SYMMETRY/ANTISYMMETRY/ ENCASTRE' in ABAQUS.

4.3. Input parameters of multi-structured knitted composite

Input parameters of the 3-D knitted composite are listed from Table 5 to Table 6. The tensile modulus and strength were provided

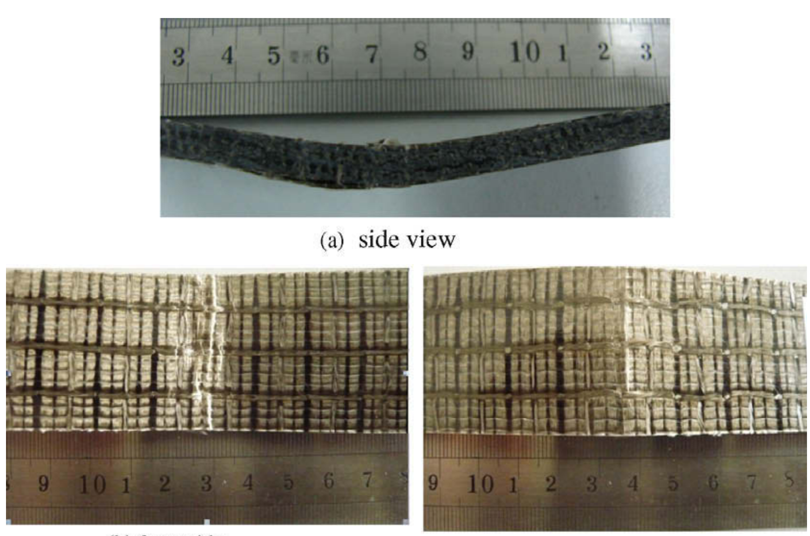

(a) side view

(b) front side

(c) rear side

Fig. 16. Quasi-static indentation damage along wale direction.

by the manufacturer of the basalt filament tows and were verified in tension testing. The other parameters were obtained from the parameters of glass fibers [26] because the basalt fibers are similar with glass fibers. The transverse parameters of the filament tow, such as G_{23} and ν_{23} are obtained from those of non-twist glass filament tows when the friction among glass fibers was considered.

5. Results and discussions

5.1. Quasi-static tests

Quasi-static indentation tests were performed on MTS810.23 material testing system with a hemispherical-end steel bar indenter. The size and shape of the steel bar is the same with that in transverse test. Fig. 11 depicts the load–displacement curves along course and wale directions (just like weft and warp direction of woven fabric) of the knitted composite.

5.2. Impact tests and FE calculation

The incident part of a stress waves recorded by gauges glued on incident bar were used as the input in dynamic FEM calculation. Fig. 10 depicts an incident part of the stress wave. The whole stress waves include input wave and reflected wave. The maximum voltage increased with the increasing of impact velocity.

Fig. 12 shows the load–displacement curves of the 3-D knitted composite along course and wale direction, respectively. The peak loads increase with the increase of impact velocities.

It can be observed a fluctuation of each load–displacement curve, which is also appeared in the result of Ji et al. [27]. The stress wave in the incident bar will hit the specimen first and induce the elastic and plastic deformation of the composite. As the stress wave reflected from the free-surface of the incident bar and the release of the elastic deformation of the composite, there is a reflective stress wave which goes through the incident bar. The reflective wave will also reflect from another free surface of the incident bar and then become the strike stress wave again. This process happens for several times until the stress wave disappears. The multi-reflective stress waves and multi-impact process are responsible for this fluctuation phenomenon.

Fig. 13 depicts the FE results of load–displacement curves. It could be shown that there are reasonable agreements between FE results and experimental. The difference between experimental and FEM is due to that all filament tows are assumed continuous and the volume fraction in each unit-cell is uniform in FEM modeling, while actually some fibers have probably been broken during fabric formation and the fiber volume fraction is not the same at different parts of the composite. Furthermore, the stress wave has different transmission speed in fiber tows and resin. Generally, the stress wave speed equals $\sqrt{E/\rho}$, where E is Young's modulus is and ρ is density. From the data in Table 5, the stress wave speed in fiber tows is 5.3 times of that in resin. This leads the local shear force at fiber–resin interface and then the local debonding. The effective stiffness will also decrease. In FE simulation, the bonding between fiber and resin is assumed perfect in unit-cell model. The shear stress generated by the different speed stress wave does not induce the interface crack. The effective stiffness under impact will maintain constant until the damages of fiber tows or matrix occur. After the breakages of fiber tows and the cracks of the matrix, the effective stiffness then will be degraded. This leads the impact force obtained from FE linearly increases until the damage occurs and decreases gradually after the partial failure of fibers and matrix.

5.3. Energy absorption

Fig. 14 compares the energy absorption of course and wale direction under different impact velocities in experiment and FE simulation. The energy absorption can be calculated from the integral of the load–displacement curves. We can find that there are good agreements between the experimental data and FE predictions. The reason for the discrepancies is due to the stiffness degradation of the unit-cell and local shear at the fiber–resin interface. The degradation of filament tows' mechanical properties should be considered in further calculation in order to improve the agreement between FE calculation and experimental results. As the impact velocity increases, the energy absorption also increases significantly. This is mainly attributed to the severe damage of the composite coupon (including fiber tows' breakage, matrix crack and composite deformation) when the impact velocity increases.

In Fig. 15, the energy absorption curves (they can also be calculated from the integral of the load–displacement curves) in the course direction increases in a step-wise function with the displacement of the transverse impact test but not in the wale direction. This is attributed to the microstructure of double-faced

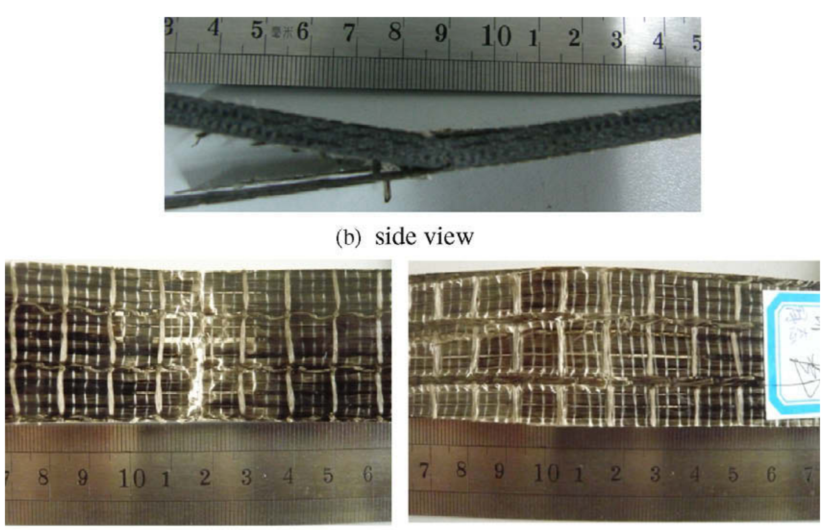

(b) side view

(b) front side

(c) rear side

Fig. 17. Quasi-static indentation damage along wale direction.

interlock knitted fabric as shown in Fig. 1. The yarn loops are oriented along wale direction. The stress waves could be transmitted along the wale direction much more smoothly than the course direction. The energy absorption along the wale direction in Fig. 15 is increased smoothly as the increase of the displacement. While along the course direction, the stress waves will be reflected along the parallel yarn loops, the energy absorption in Fig. 15 will be increased in the each step of wave reflection and in a step-wise way.

5.4. Failure mode

In the quasi-static test, tensile failure mode is dominant on the rear side, but in the high velocity impact test, resin spallation failure mode could be found on the rear side. Figs. 16 and 17 show these impact damage modes along wale and course direction, respectively.

Fig. 18 depicts the impact damage development of the composite under impact loading. Fig. 19 is the impact damage of the knitted composite at front side and rear side in the impact velocity of 20.0 m/s. Fig. 20 is the transverse impact damage evolution of the 3-D knitted composite in experimental and FE simulation. As the impact velocity increases, the damage area of the composites specimen becomes larger because higher energy absorption. For example, the damage area is 34.4 mm^2 for 17.5 m/s and 45.2 mm^2 for 22.5 m/s as shown in Fig. 21. Resin crack is the main damage mode on the front surface under transverse impact both along course and wale direction. Fiber breakage and resin spallation are the main damage mechanism in the rear surface. The reason for the matrix spallation at the rear surface is that stress waves propagate from the front surface to rear surface and then reflect from the rear surface. This will deduce the double stress amplitude which leads the matrix spallation which often occurred in ballistic impact. Furthermore, the multi-structured knitted composites have high delami-

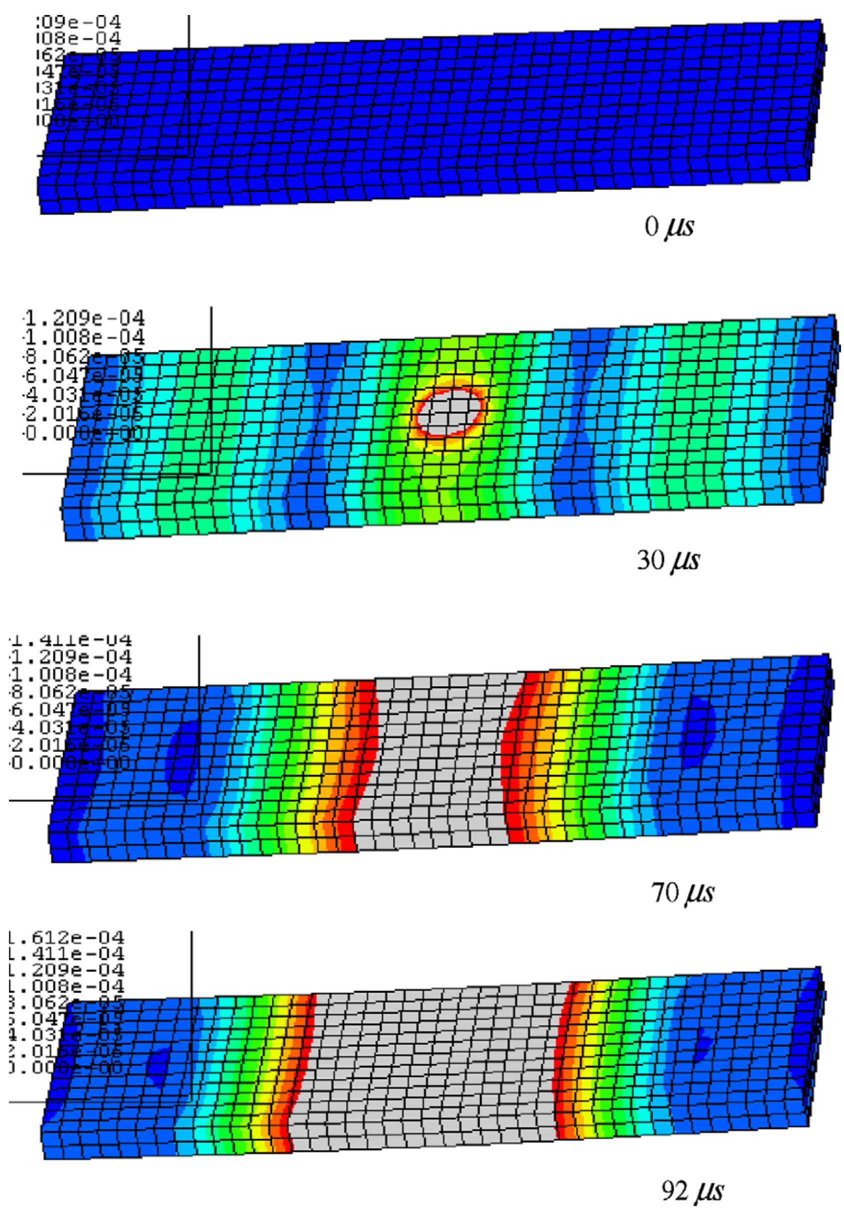

Fig. 18. FEM results of impact damage evolution of the knitted composite.

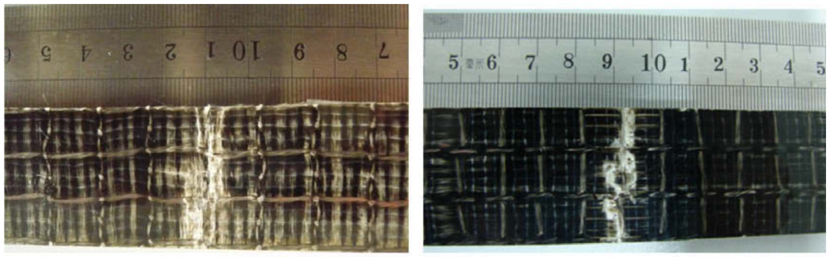

(a) front side (b) rear side

Fig. 19. Impact damage of knitted composite at the impact velocities of 20.0 m/s.

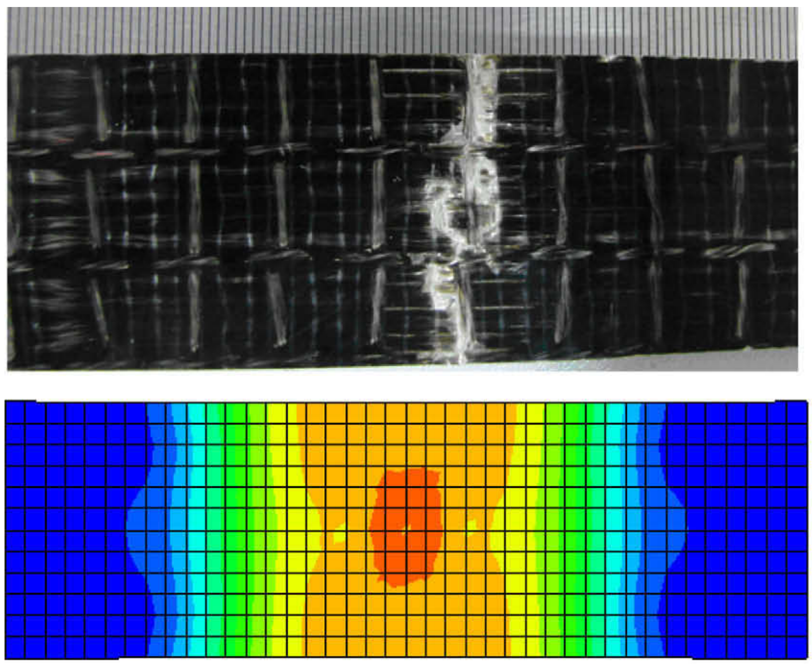

(a) course direction

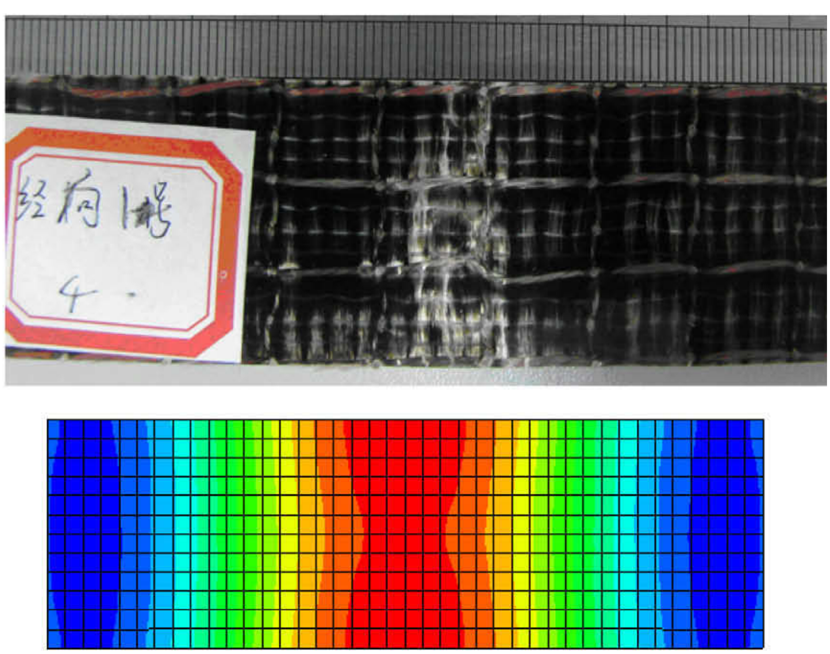

(b) wale direction

Fig. 20. Comparisons of impact damage between experimental and theoretical.

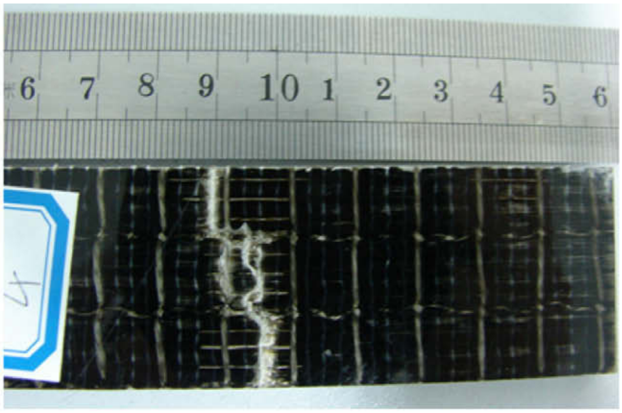

(a) 17.5m/s

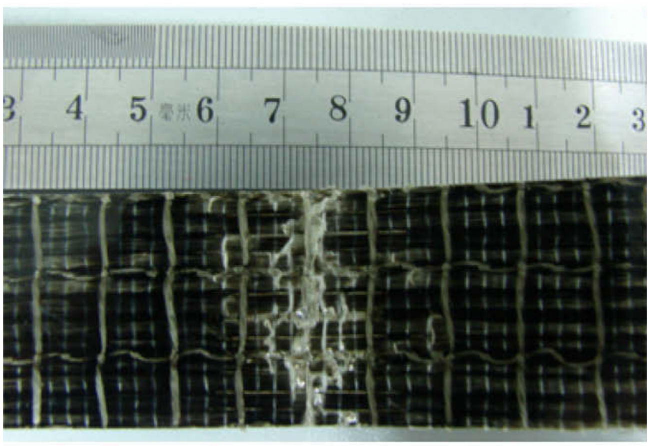

(c) 22.5m/s

Fig. 21. Comparison of damage areas under different impact velocities at rear side.

nation resistance because no delamination is found in both quasi-static loading and high velocity impact tests.

6. Conclusions

Mechanical behaviors and damage modes of multi-structured knitted composites under quasi-static (2 mm/min) and transverse impact loading along course and wale directions were tested with MTS810.23 materials tester and a modified split Hopkinson pressure bar (SHPB) apparatus. The load–displacement curves of the multi-structured knitted composites under different velocities impact were obtained to calculate the energy absorption of the composites. We found the energy absorption of the composites increase as the impact velocity increases. The composites have almost same energy absorption along warp and weft directions. The morphologies of the damaged composite specimens show the different failure modes under quasi-static test and high velocity impact. In quasi-static test, the failure mode is compressive failure on the front side and tensile failure on the rear side. Resin spallation could be found on the rear surface under transverse impact. Based on the unit-cell model of the 3-D knitted composite, a user-defined materials' subroutine VUMAT was developed and combined with ABAQUS/Explicit to calculate load vs. displacement curves of transverse impact loading. The load–displacement curves, impact damages and impact energy absorptions calculated with ABAQUS are compared with those in experiments. The good agreements of the comparisons prove the validity of the unit-cell model and user-defined subroutine. The unit-cell model can also be extended to the impact crashworthiness simulation of engineering structures made of the 3-D knitted composite.

Acknowledgements

The authors acknowledge the financial supports from the National Science Foundation of China (Grant Nos. 50675032, 10802022 and 10872049) and the Key-grant Project of Chinese Ministry of Education (No 309014). The sponsors from Shanghai Educational Development Foundation (08CG39) and Shanghai Rising-Star Program (08QA14008) are also gratefully acknowledged.

References

[1] Pandita S D, Falconet D, Verpoest I. Impact properties of weft knitted fabric reinforced composites. Compos Sci Technol 2002;62:1113–23.
[2] Khondker OA, Herszberg I, Hamada H. Measurements and prediction of the compression-after-impact strength of glass knitted textile composites. Composites A 2004;35:145–57.
[3] Khondker O A, Fukui T, Nakai A, Hamada H. Initial fracture of the welt weft-knitted textile composites. Composites A 2004;35:1185–94.
[4] Khondker O A, Fukui T, Inoda M, Nakai A, Hamada H. Fabrication and mechanical properties of aramid/nylon plain knitted composites. Composites A 2004;35:1195–205.
[5] Khondker O A, Leong K H, Herszberg I, Hamada H. Impact and compression-after-impact performance of weft-knitted glass textile composites. Composites A 2005;36:638–48.
[6] Ramakrishna S, Hamada H, Rydin RW, Chou TW. Impact damage resistance of knitted glass-fiber fabric reinforced polypropylene composites. Sci Eng Compos Mater 1995;4(2):61–72.
[7] Kang TJ, Kim C. Mechanical and impact properties of composite laminates reinforced with Kevlar multiaxial warp knit fabrics. Polym Polym Compos 1997;5(4):265–72.
[8] Kang TJ, Kim C. Energy-absorption mechanisms in Kevlar multiaxial warp-knit fabric composites under impact loading. Compos Sci Technol 2000;60(5):773–84.
[9] Cox B N, Davis J B. Knitted composites for energy absorption under tensile loading. Composites A 2001;32:91–105.
[10] Lam SW, Tao XM, Yu T. Comparison of different thermoplastic cellular textile composites on their energy absorption capacity. Compos Sci Technol 2004;64(13–14):2177–84.
[11] Putnoki I, Moos E, Karger-Kocsis J. Mechanical performance of stretched knitted fabric glass fibre reinforced poly(ethylene terephthalate) composites produced from commingled yarn. Plast Rubber Compos 1999;28(1):40–6.
[12] Sugun BS, Rao RMVGK. Drop weight impact studies on rib-knit RTM laminates. J Reinforc Plast Compos 2000;19(6):492–508.
[13] Zhou RX, Hu H, Chen NL, Feng XW. An experimental and numerical study on the impact energy absorption characteristics of the multiaxial warp knitted (MWK) reinforced composites. J Compos Mater 2005;39(6):525–42.
[14] Huang Z M. Progressive flexural failure analysis of laminated composites with knitted fabric reinforcement. Mech Mater 2004;36:239–60.
[15] Sun B Z, Hu H, Gu B H. Compressive behavior of multi-axial multi-layer warp knitted (MMWK) fabric composite at various strain rates. Compos Struct 2007;78(1):84–90.
[16] Liu Y W, Lv L H, Sun B Z, Hu H, Gu B H. Dynamic response of 3D biaxial spacer weft-knitted composite under transverse impact. J Reinforc Plast Compos 2006;25(15):1629–41.
[17] Hao AY, Sun BZ, Qiu YP, Gu BH. Dynamic properties of 3-D orthogonal woven composite T-beam under transverse impact. Composites A 2008;39(7):1073–82.
[18] Meyers MA. Dynamic behavior of materials. In: Experimental techniques: methods to produce dynamic formation. New York: John Wiley & Sons, Inc.; 1994. p. 296–322 [chapter 12].
[19] Ko FK. Three-dimensional fabrics for composites. In: Chou TW, Ko FK, editors. Textile structural composites. Amsterdam: Elsevier Science Publishers B.V.; 1989. p. 140–2.
[20] Cox BN. On the tensile failure of 3D woven composites. Composites A 1996;27(6):447–58.
[21] Hahn HT, Tsai SW. Nonlinear elastic behavior of unidirectional composite laminae. J Compos Mater 1973;7(1):102–18.
[22] Hahn HT. Nonlinear behavior of laminated composites. J Compos Mater 1973;7(2):257–71.
[23] Rosen BW. Tension failure of fibrous composites. AIAA J 1964;2(11):1985–91.
[24] 24 Gucer DE, Gurland J. Comparison of the statistics of two fracture modes. J Mech Phys Solids 1962;10(4):285–376.
[25] Chang FK, Chang KY. Post-failure analysis of bolted composite joints in tension or shear-out mode failure. J Compos Mater 1987;21(9):809–27.
[26] Morton WE, Hearle JWS. Physical properties of textile fibres. 2nd ed. London: William Heinemann Ltd; 1975. p. 399–440.
[27] Ji KH, Kim SJ. Dynamic direct numerical simulation of woven composites for low-velocity impact. J Compos Mater 2007;41(2):175–200.